Research paper

A synergistic effect of Co and CeO$_2$ in nitrogen-doped carbon nanostructure for the enhanced oxygen electrode activity and stability

Arumugam Sivanantham, Pandian Ganesan, Sangaraju Shanmugam*

Department of Energy Systems Engineering, Daegu Gyeongbuk Institute of Science & Technology (DGIST), Daegu, 42988, Republic of Korea

A B S T R A C T

The development of efficient and durable non-precious cathode catalyst have been received the great interest to replace the commercial noble catalysts, thereby minimizing the overall cost of polymer electrolyte membrane fuel cells. We describe the synthesis of self-redox CeO$_2$ supported Co in nitrogen-doped carbon nanorods (Co-CeO$_2$/N-CNR) by the electro-spun method, and introduced as an enhanced bifunctional catalyst for oxygen reduction (ORR) as well as evolution (OER) reactions by the synergistic effect of oxygen buffer CeO$_2$ with metallic Co. Systematic structural and optical studies confirm the formation and uniform distribution of CeO$_2$ and Co particles in N-CNR. The X-ray photoelectron spectroscopy analysis of Co-CeO$_2$/N-CNR reveals that the presence of Co^{2+} and multiple valence states of ceria (Ce^{4+} and Ce^{3+}). The shift in binding energies of Co^{2+} and Ce^{3+} states confirm the possible interaction for the cooperative effect of ceria and cobalt during ORR and OER, and electrode stability improvement as well. The Co-CeO$_2$/N-CNR catalyst shows the enhanced oxygen electrode potential of 0.84 V (versus reversible hydrogen electrode), which is 100 and 196 mV lower than Co/N-CNR and Pt/C, respectively, including the improved stability.

1. Introduction

Platinum group metal (PGM) based renewable technology requires two key changes: (1) most active and stable PGM-free catalysts and (2) poison additives free fuels for new technology developments [1,2]. In particular, oxygen reduction (ORR) and evolution (OER) reactions have been received an extensive attention due to the principal role in energy conversion and storage devices, such as fuel cells, water electrolyzers, batteries, etc [3–7]. Both reactions occur on the catalysts surface at higher positive potential. So, ultimately the catalysts should endure the activity or stability difficulties (loss) [8,9].

So far, the different materials have been explored as the supported catalysts to enhance the ORR and OER activity, including the carbon with different morphologies [10–13]. Widely, the metal oxides have been introduced as the supported catalysts due to their chemical stability and robustness at the higher potential and the harsh electrolyte environment as well [14,15]. However, most of the supported metal oxides are helped to improve the catalyst activity or stability, sometimes it could not provide the good support effect due to the following features: (i) no or improper interaction with the metal catalyst particle; (ii) easy detachment from the catalyst surface during the electrochemical performance; and (iii) electrochemically less active property [16,17]. These limitations led us to develop the alternative catalysts which can provide the enhanced electrochemical activity and the stability as well.

In line, ceria (CeO$_2$) is an environmentally benign and technologically important low-cost semiconducting material due to the reversible conversion to a nonstoichiometric oxide [18]. Especially, CeO$_2$ exhibits the proper redox features. So, it possesses more oxygen vacancy defects, excellent catalytic oxidation property, enormous oxygen utilization capability and reversible conversion between the oxidation states of Ce^{3+} and Ce^{4+} [19,20]. The oxygen vacancies of ceria are responsible for the favorable physicochemical properties, including the good chemical and mechanical stability. So, the ceria is considered as one of the promising oxygen buffer materials in catalysis and optoelectronic applications [21–23].

Recently, CeO$_2$ has been explored as potentially supported candidate for the catalysis applications owing to its moderate band gap, multiple valence states and oxygen ion conductivity, which might be suitable for the enhanced oxygen electrode activities [24,25]. It is believed that the enhanced catalytic activity and stability are associated with the supported catalysts self-redox property, continuous motion of electrons by rapid formation and elimination of oxygen vacancy defects and their stability to improve the higher oxygen translate capacity in oxygen reduction and evolution processes [26]. For instance, Yu et al., explored the CeO$_2$ as a cathode catalyst in lithium-air battery due to the

---

easy transformation of reduction and oxidation states [27]. Recently, Kim et al., reported the synthesis of Co and CeO_2 doped carbon nanofiber and used as an electrode in supercapacitor [28]. Also, Zhu et al., studied that the CeO_2 severs as good support for precious RuO_2 for enhanced and stable water oxidation due to the self-redox property of CeO_2 [29].

Herein, we have introduced the CeO_2 supported Co/N-CNR as an efficient and durable catalyst for both ORR and OER due to the co-operative effect of lower oxidation state (Ce^{3+}) of ceria with cobalt metal. The Co-CeO_2/N-CNR (CC: cobalt-cerium) is fabricated by the two-step method of electro-spun, followed by annealing in ambient atmospheres. As-prepared Co-CeO_2/N-CNR exhibits the enhanced bi-functional activity and stability than the Co/N-CNR and Pt/C catalysts. The Co-CeO_2/N-CNR catalyst shows the oxygen electrode potential of 0.84 V, which is much lower than the all other catalysts. Besides, Co-CeO_2/N-CNR catalyst shows the improvement in both ORR and OER stability. As a result, the CeO_2 is one of the most suitable supported catalysts to enhance the Co/N-CNR catalyst electrochemical activity and the stability as well.

2. Experimental section

2.1. Materials

Polyacrylonitrile (PAN, average MW = 150,000), cobalt (II) acetylacetonate (Aldrich, $C_{10}H_{14}CoO_4$), cerium (III) acetylacetonate (Aldrich, $C_{15}H_{21}CeO_6 \cdot xH_2O$), dimethyl formamide (DMF, Daejung, $HCON(CH_3)_2$), aluminum foil and syringe (12 mL, NORM-JECT). All the chemicals and solvent are used without additional treatment.

2.2. Synthesis of Co-CeO₂/N-CNR electrocatalyst

Initially, the precursors of polyacrylonitrile, cobalt (II) and cerium (III) acetylacetonates (ratio of 8:1:1) is added with 10 mL dimethyl formamide and stirred at 80 °C for the overnight. Next, the clear solution filled syringe is fixed in the electro-spun set up (eS-robot electrospinning system). Then, the polymer fiber mat is electrospun on the aluminum foil at the applied voltage of 12 ± 2 kV between the 10 cm distanced anode and cathode. The mat is peeled off from the aluminum foil and then pyrolyzed in the tubular furnace (Wisetherm) using a silicon crucible at 300 °C for 3 h in open air, followed by the annealing at various temperatures (850 and 900 °C) and times (1 and 2 h) in argon (Ar) atmosphere. According to the temperature and time, the catalysts were named as CC1 [Co-CeO_2/N-CNR at 900 °C (2 h)], CC2 [Co-CeO_2/N-CNR at 900 °C (1 h)] and CC3 [Co-CeO_2/N-CNR at 850 °C (2 h)]. Similarly, the Co/N-CNR and CeO_2/N-CNR are formed without cerium and cobalt precursors, respectively. The N-CNR is synthesized from PAN without any metal precursors. As-prepared catalysts are used for all the characterizations and electrochemical tests.

2.3. Characterizations

Catalysts phase formation and the graphitic/amorphous nature of carbon is confirmed using the X-ray diffraction spectroscopy as well as Raman spectroscopy (514 nm laser wavelength). The morphology and surface nature are analyzed by scanning electron microscopy (S4800) and the transmission electron microscopy (HF 3600) techniques. Bruner–Emmett–Teller (Micromeritics ASAP 2020) is employed for the surface area measurement; including the pore diameter information from the t-plot technique using Harkins-Jura principle. For all catalysts the BET measurement is carried out after degassing at 250 °C for 2 h. The quantitative analysis of C, N, and H (heteroatom functionalities) is done by the elemental analyzer (Vario MICRI cube). The chemical composition nature of various elements in the different catalysts is examined by the X-ray photoelectron spectroscopy (Thermo Scientific ESCALAB 250Xi).

2.4. Electrochemical measurements

Using a bi-potentiostat (Biologic, VSP-Modular 2 channels) all the electrochemical measurements are carried out with the help of commercial three electrodes set-up in the aqueous electrolyte of 0.1 M KOH. The glassy carbon rotating disk, platinum wire, including saturated calomel electrode are used as a working, counter and reference electrodes, respectively. For the catalyst ink preparation, the catalyst (1.5 mg) is dispersed in 1:3:16 ratios of Nafion, de-ionized water, and isopropyl alcohol, respectively. A catalyst loading of 0.21 mg cm^{-2} is maintained for all the electrochemical measurements. Similarly, the precious catalyst of Pt/C(10%) ink is prepared and maintained the loading amount of 0.21 mg cm^{-2}. Before the ORR performance, the O_2 gas is purged for 30 min in the electrolyte solution. The RDE electrode is rotated at a constant speed of 1600 rpm during the measurements. The scan rate is 10 mV s^{-1} and all the potential scale values are converted to the reversible hydrogen electrode (RHE) using reference electrode calibration potential value. The Ar-corrected current density values are displayed in all the ORR linear sweep voltammogram (LSV) curves. Similarly, the OER potential values in LSV curves are iR-compensated by the ohmic resistance (R_s) value. The current density is calculated based on geometrical surface area. Electrochemical impedance spectroscopy study is carried out at 1.489 V vs. RHE with the frequency range of 200 kHz to 100 mHz. The electrochemically active surface is measured from the electrical double layer capacitance measurements, for that the cyclic voltammetry is cycled at 20, 40, 60, 80 and 100 mV s^{-1} (scan rates) between 1.24 and 1.34 V vs. RHE. The number of electrons transfer during ORR is measured from the Koutecky–Levich (K-L) plot, which is determined by the following equation.

$$1/J = 1/J_L + 1/J_K = 1/B\omega^{1/2} + 1/J_K$$

$$B = 0.62 \ n \ F \ C_o \ D_o^{2/3} \ \nu^{-1/6} \tag{1}$$

Where, J, J_L and J_K are the experimentally measured current, diffusion-limiting current and kinetic current values, respectively. Also, the representations of ω and F are the angular velocity and Faraday constant values, respectively. The saturated concentration and diffusion coefficient values of O_2 are 1.2×10^{-6} mol/cm^3 (C_0) and D_0 1.9×10^{-5} cm^2/s^1 (D_0), respectively in 0.1 M KOH. Besides, ν is the electrolyte kinematic viscosity and the number of electron "n" can be calculated from the slope of J^{-1} vs. $\omega^{-1/2}$ plot.

3. Results and discussion

3.1. Formation of the nanostructured catalysts via electrospinning

The schematic illustration of the formation of various catalysts is shown in Fig. 1. First, the precursors of polyacrylonitrile, Co and Ce acetylacetonates are completely dissolved in dimethyl formamide solvent on the catalysts at 80 °C. Then, the solution is filled in a syringe and electrospun on aluminum current collector with the applied voltage of 12 ± 2 kV. Next, the electrospun polymer mat is heated in a tubular furnace at different temperatures with various time durations to obtain a serious of catalysts (see the experimental section). The Fig. 1 displays the 3D crystal structure of Co, CeO_2, and Co-CeO_2 from the Co/N-CNR, CeO_2/N-CNR, and Co-CeO_2/N-CNR catalysts, respectively.

3.2. Characterizations of catalysts

3.2.1. XRD analysis

The XRD patterns as shown in Fig. 2 display the phase formation of different catalysts, including the nature of carbon before and after metal/metal oxide incorporation. The N-CNR catalyst shows the broad XRD peaks at 2θ values of 24.2° and 44.5° for C(002) and C(100), respectively and also confirms the amorphous nature of carbon (Fig. 2a).
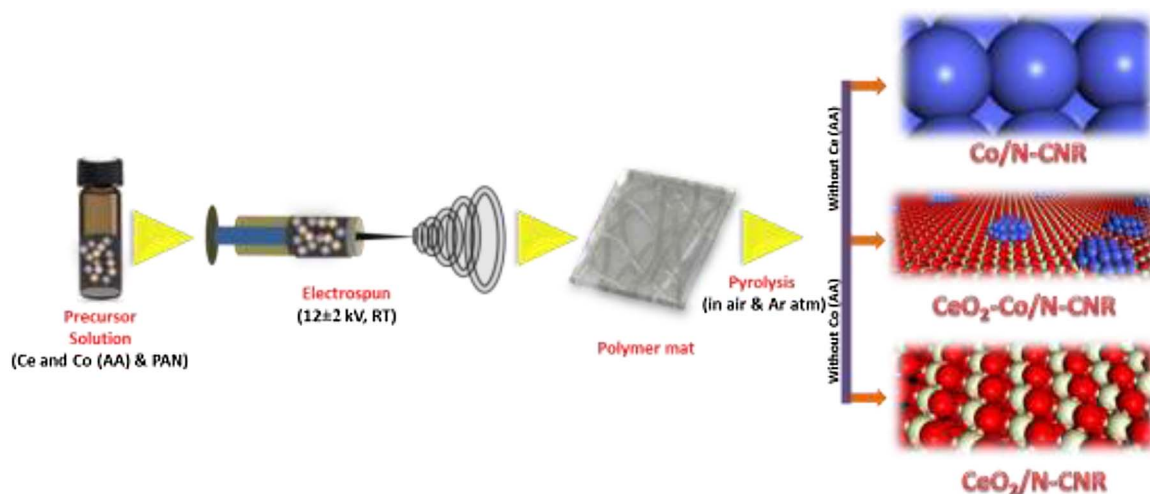
Fig. 1. Illustration of Co/N-CNR, CeO$_2$/N-CNR and Co-CeO$_2$/N-CNR catalysts formation by the electrospun method, followed by annealing.
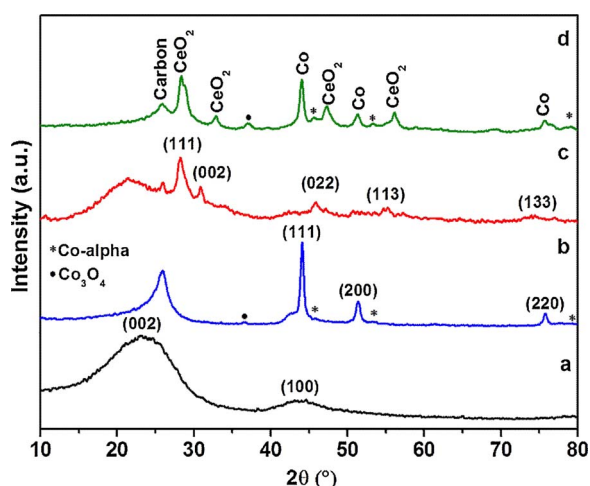

Fig. 2. XRD patterns of (a) N-CNR, (b) Co/N-CNR, (c) CeO$_2$/N-CNR, and (d) Co-CeO$_2$/N-CNR (CC1) catalysts.

The XRD pattern of Co/N-CNR (Fig. 2b) shows three strong peaks at 44.4°, 52.2° and 76.3° correspond to the (111), (200) and (022) planes of Co metal with cubic phase (JCPDS: 98-062-2434), including smaller amount cobalt alpha (asterisk) phase (JCPDS: 98-004-1507) and Co$_3$O$_4$ (~2%, dot). Also, the sharp peak at 25.1° confirms the change of carbon nature from amorphous to graphitic. In Fig. 2c, the XRD result of CeO$_2$ incorporated N-CNR (CeO$_2$/N-CNR) exhibits different diffraction peaks at 29.4°, 30.9°, 46.3°, 57.2° and 74.5° correspond to the formation of cubic CeO$_2$ (JCPDS: 98-015-5608) with (111), (002), (022), (113) and (133) planes, respectively. Interestingly, the CeO$_2$ in N-CNR has a minor amount of graphitic carbon (not like Co metal), it confirms by the less peak boarding at 24.2°. The XRD pattern of Co-CeO$_2$/N-CNR (CC1) displays various peaks which we observe from two different catalysts of Co (including cobalt-alpha) and CeO$_2$, including the partially graphitic carbon peaks. It indicates that the both Co metal (64%) and CeO$_2$ (36%) are present in the Co-CeO$_2$/N-CNR catalyst (Fig. 2d). The sharp peak at 25.1° with less base boarding reveals the presence of carbon with more graphitic nature in the CC1 catalyst. Furthermore, the small positive peak shift has observed in all the peaks of CeO$_2$ catalyst, which reveals the possible interaction of CeO$_2$ with Co metal. Similar XRD patterns are observed for all other controlled catalysts (CC2 and CC3), but the CC3 catalyst exhibits more amorphous carbon due to the lower annealing temperature of 850 °C (Fig. S1). Also, the small peak intensity increment (~3%) of Co$_3$O$_4$ (dot) is noticed in all the Co-CeO$_2$/N-CNR catalysts than Co/N-CNR catalyst, which may be due to the presence of surrounding CeO$_2$.
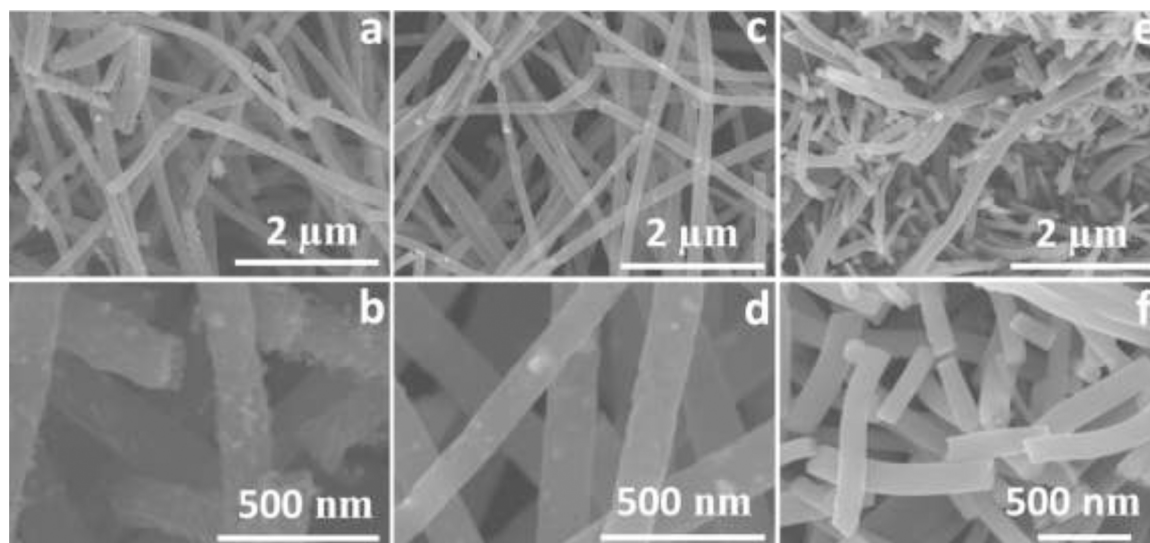

Fig. 3. FE-SEM (low and high magnification) images of (a,b) Co-CeO$_2$/N-CNR (CC1), (c,d) Co/N-CNR, and (e,f) CeO$_2$/N-CNR catalysts.

3.2.2. SEM analysis

Figs. 3 and S2 display the FE-SEM images and surface property of the different catalysts. Moreover, all the catalysts exhibit nanorod-like morphology with the average diameter of ~150 nm and length of ~2 μm. As shown in Fig. 3a and b, the CeO_2 supported Co/N-CNR reveals the existence of nanoparticles on the surface of carbon nanorods with the diameter range of 10–20 nm. Also, the catalyst surface has more roughness, which can increase the active sites and may have good electrolyte utilization nature [30]. Similar morphology is observed for other Co-CeO_2/N-CNR (CC2 and CC3) catalysts (Fig. S2a–d). However, the absence of CeO_2 in Co/N-CNR (Fig. 3c and d) has a smooth surface and less existence of nanoparticles with the diameter range of 20–40 nm. Nevertheless, the CeO_2/N-CNR (Fig. 3e and f) and N-CNR (Fig. S2e and f) provide a smoother surface than the Co-CeO_2/N-CNR and Co/N-CNR catalysts. Hence, CeO_2 incorporation in the Co/N-CNR improves the surface area and the electrochemical active sites as well, which will be discussed in the subsequent sections based on the BET and ECSA results.

3.2.3. TEM analysis

Furthermore, the TEM and HR-TEM analyses combined with elemental mapping are explored to understand the morphology of distributed CeO_2, Co metal and carbon with their crystalline nature in Co-CeO_2/N-CNR (CC1), displayed in Fig. 4. Again, the TEM image confirms the nanorod morphology of catalyst with the uniform distribution of both Co and CeO_2 nanoparticles in the carbon nanorod (Fig. 4a). The dark spots are attributed to the Co nanoparticles, and the brighter contrast spots (due to the less surface charge) show the occurrence of CeO_2 nanoparticles. In Fig. 4b, the HR-TEM image represents the crystalline nature of CeO_2, Co and carbon with different d-spacing values as marked in the image. The measured d-spacing values of 0.2 and 0.31 nm corresponding to the d-spacing values of (111) plane of both Co and CeO_2 cubic crystals, respectively [31]. Mostly, both CeO_2 and Co nanoparticles are covered with the amorphous carbon, including a small amount of graphitic carbon. The STEM elemental mapping results as shown in Fig. 4c–h reveal that the Ce (Sky Blue), Co (Red), O (Green) C (Pink) and N (Blue) elements are uniformly distributed in the entire nanorod.

3.2.4. BET analysis

The BET isotherms and the pore size distribution of catalysts are shown in Figs. 5 and S3 . Mostly, all the catalysts exhibit the type-IV isotherms, indicating that the existence of mesoporous structure [32]. The BET specific surface area values of 464, 412, 101 and 28 $m^2 g^{-1}$ are observed from the Co-CeO_2/N-CNR, Co/N-CNR, CeO_2/N-CNR and N-CNR, respectively. The surface area of N-CNR (28 $m^2 g^{-1}$) is increased four times due to the CeO_2 nanoparticles incorporation. Comparatively, the CeO_2 supported Co/N-CNR (CC1) has high surface area than all other catalysts, it confirms the role of CeO_2 in the catalyst surface area enhancement. The pore size distribution for all the catalysts are obtained from the t-plot and shown in Fig. S3 [33]. The catalysts of Co-CeO_2/N-CNR (CC1), Co/N-CNR, CeO_2/N-CNR and N-CNR display the small mesoporous size of 3.9, 3.7, 3.5 and 3.7 nm, respectively. Hence, the specific surface area of Co/N-CNR is increased owing to the incorporation of CeO_2 and the BET results have good agreement with the FE-SEM morphology.
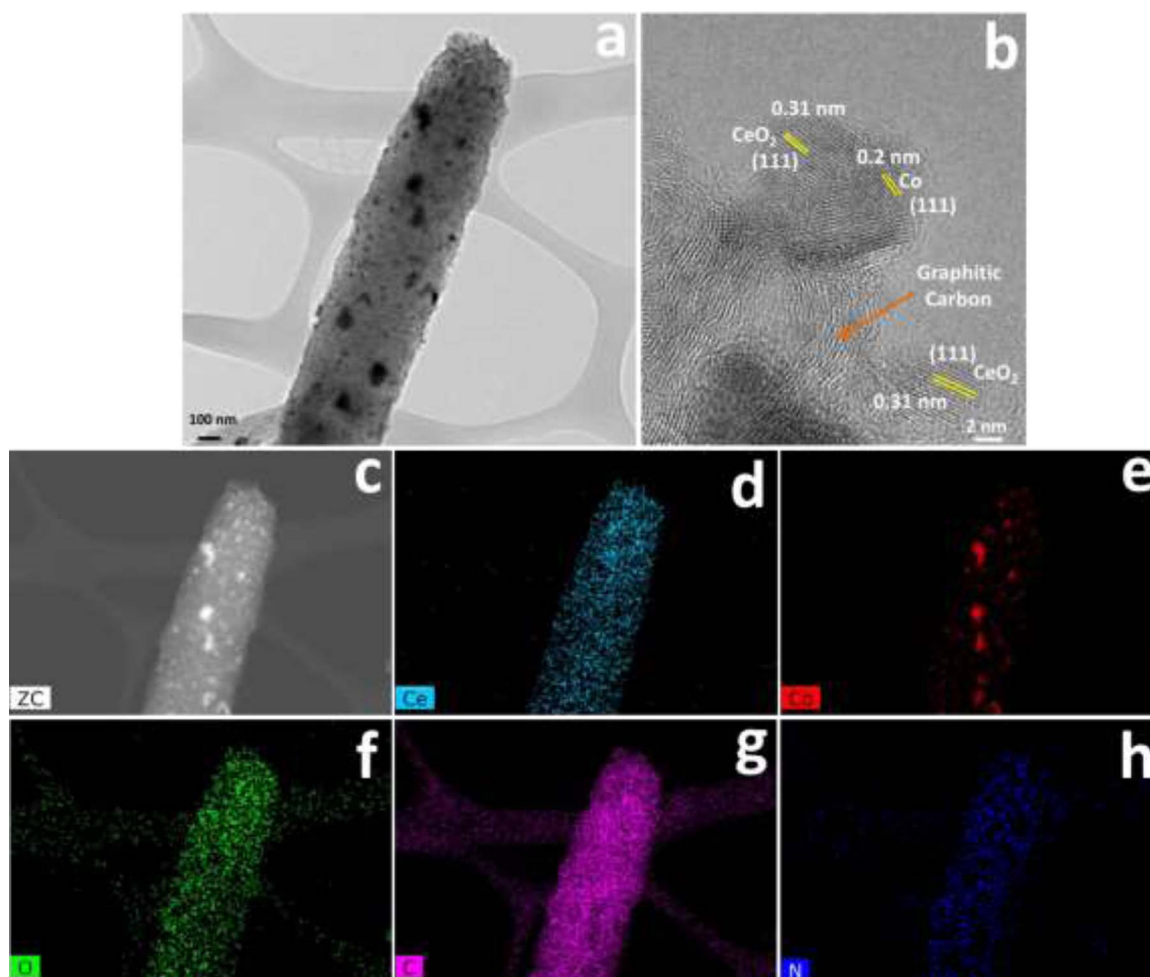

Fig. 4. (a) TEM image, (b) HR-TEM image with lattice fringes, (c) STEM image and (d-h) elemental mapping of Ce, Co, O, C and N, respectively, for the Co-CeO_2/N-CNR (CC1).
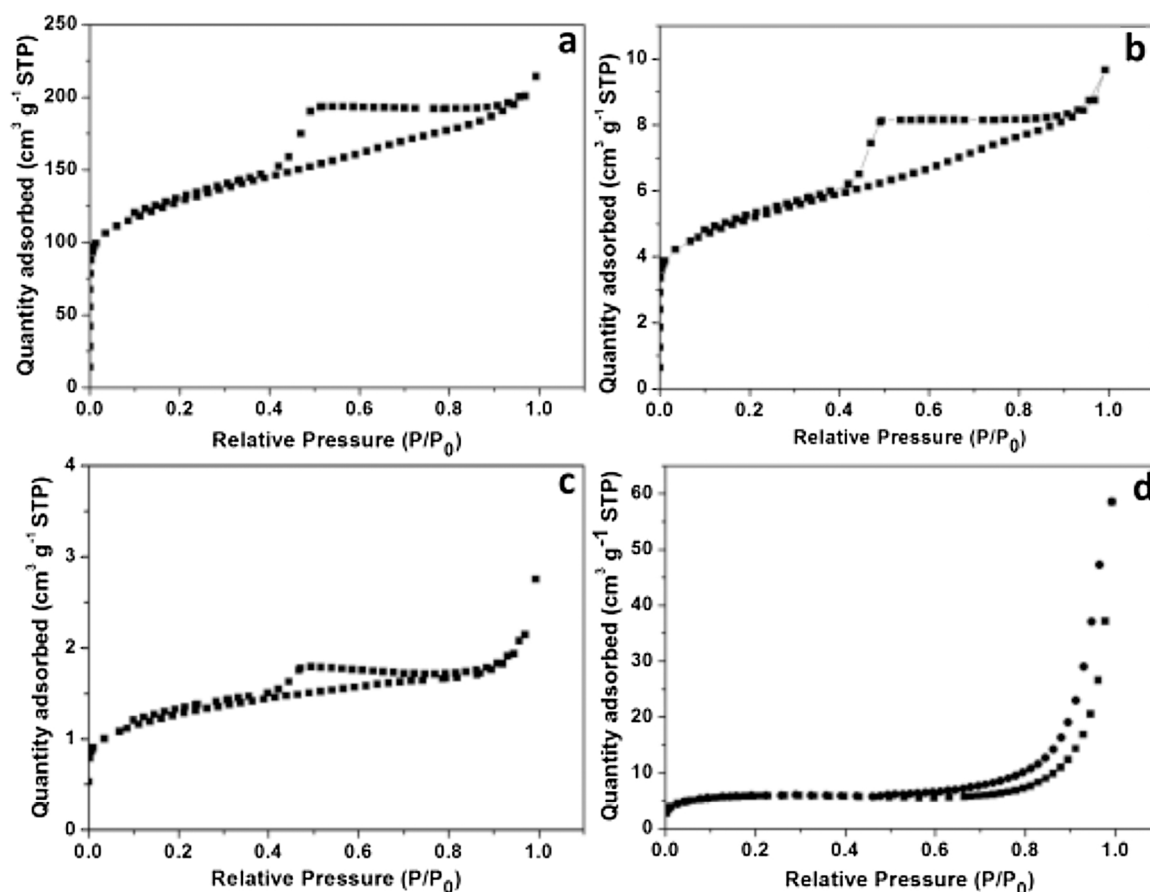
Fig. 5. BET surface area analysis: N_2 adsorption − desorption isotherms of (a) Co-CeO$_2$/N-CNR (CC1), (b) Co/N-CNR, (c) CeO$_2$/N-CNR and (d) N-CNR catalysts.

3.2.5. XPS analysis

For further insight on surface chemical composition and other functional groups of Co-CeO$_2$/N-CNR (CC1), the X-ray photoelectron spectroscopy (XPS) analysis was executed and results are shown in Fig. 6. Also, the other catalysts XPS spectra were compared and shown in Figs. S4–S6. As shown in Fig. 6a, the five deconvoluted XPS peaks of the C1s reveal the nature of carbon and their bonding with nitrogen and oxygen elements. The intense peak at 284.6 eV (C1) indicates the presence of sp^2 non-oxygenated/aromatic carbon ring (C−C), which is a signature for the graphitic carbon [34,35]. The next higher binding energy peak at 285.6 eV (C2) refers to the C−N bond, other two small intensity peaks located at 286.2 (C3) and 287.5 (C4) are attributed to C−O and C=O bonds, due to the oxygenated carbon surface [36,37]. The broad peak (C5) at the binding energy of 291.0 eV is the shake-up satellite peak [38]. The comparison catalysts (N-CNR, Co/N-CNR, and CeO$_2$/N-CNR) also exhibit the five deconvoluted peaks at the similar binding energies as discussed above with small intensity variation, which is displayed in supporting information (Fig. S4a–c).

Fig. 6b shows the deconvoluted N1s spectrum with four kinds of nitrogen bonding with carbon. The maximum intensity peak at 400.8 eV (N1) is due to the presence quaternary nitrogen groups [39,40]. The replacement of C atom by quaternary-N in the hexagonal carbon ring can improve the carbon charge density, and it could increase the conductivity of carbon nanorods by the reduction of energy gap among the highest occupied molecular orbital (HOMO) and lowest occupied molecular orbital (LOMO) [32]. The peak at a binding energy value of 398.1 eV (N2) corresponds to the pyridinic-N group, this nucleophilic species bonded to two sp^2 carbons at the edge sites with one lone pair of electrons [41]. The localized electron pair of pyridinic-N's can easily interact with oxygen/protons species, and which behaves like a basic site for electrophilic substitution or elimination reactions [42].

The other two peaks N3 (399.8 eV) and N4 (398.8 eV) relate to pyrrolic-N and pyrrolidonic-N moieties. The pyrrolic-N contributes its lone pair of electrons to aromatic π-carbon ring at the edge of sp^2 carbon frameworks; it can generate a negative charge in the carbon framework [43]. Also, the comparison catalysts exhibit the similar N1s spectrum (Fig. S4d–f), it confirms that the carbon nanorods have less energy gap and excellent conductivity towards electron movements.

The Co2p XPS spectrum was deconvoluted into one spin-orbit doublet with their corresponding shake-up satellite peaks (Fig. 6c). The broad Co2p$_{3/2}$ peak at the binding energy of 780.99 eV and the satellite peak at 786.3 eV confirm the Co^{2+} oxidation state, due to the surface hydroxide formation from the moisture [31,44]. Their corresponding doublet peak Co2p$_{1/2}$ at 796.4 eV is confirmed from the binding energy difference of 15.4 eV [45,46]. The fitted XPS spectra of Co/N-CNR catalyst also confirm the Co^{2+} oxidation state (Fig. S5a). However, when the CeO$_2$ is incorporated in Co/N-CNR, the spin-orbit doublet peak has a positive shift of ∼0.2 eV. It implies that the CeO$_2$ has direct or indirect interaction with Co metal which shifted the Co metal binding energy.

Fig. 6d depicts the Ce3d level spectrum and fitted with eight characteristic peaks for four pairs of spin-orbit doublets. The peaks represented as u (882.6 eV), u' (885.7 eV), u'' (888.8 eV) and u''' (898.4 eV) belong to the components of Ce3d$_{5/2}$, and the peaks marked as v (901.1 eV), v' (904.1), v'' (907.3 eV) and v''' (916.8 eV) correspond to the components of Ce3d$_{3/2}$ [47]. The peaks u' (904.1 eV) and v (885.7 eV) attribute to the Ce^{3+}3d$_{3/2}$ and Ce^{3+}3d$_{5/2}$ (3d^{10}4f^1 initial electronic state), respectively, and the other peaks attribute to the Ce^{4+} (3d^{10}4f^0 initial electronic state), which indicates the coexistence of Ce^{3+} and Ce^{4+} valance states [48]. Interestingly, the Ce^{3+} ions contribute in the interaction between ceria and surrounding atoms such as Co through the lone electron which presents in the 4f^1 orbital. Also, due
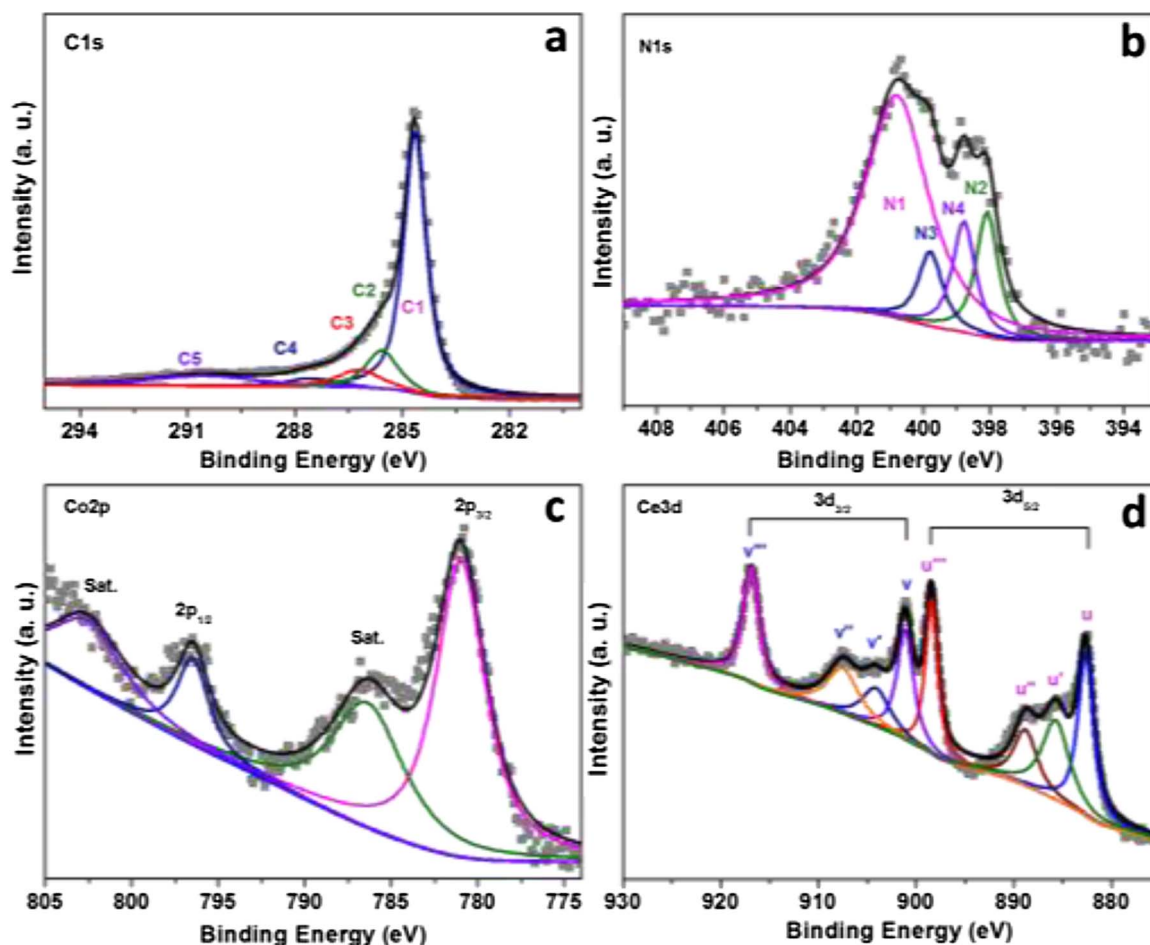
Fig. 6. High resolution XPS de-convolution spectra of (a) C1s, (b) N1s, (c) Co2p and (d) Ce3d for Co-CeO$_2$/N-CNR (CC1) catalyst.

to the charge compensation of Ce^{3+} ions, which can generate an oxygen vacancies and increase the oxygen absorbance on the catalyst surface [40]. Also, the ceria can donate the lattice oxygen to the cobalt, which can retain the cobalt ion in the higher valence state [49]. The CeO$_2$/N-CNR catalyst also exhibits the both Ce^{3+} and Ce^{4+} oxidation peaks (Fig. S5b). However, a small positive shift has noticed in the ceria peaks, particularly in Ce^{3+}, it indicates the possible electrostatic interaction of ceria with surrounding Co metal. This result has good concurrence with the XRD observations. The active phase of Co metal interaction with support can strongly influence in the catalytic performance of Co-CeO$_2$/N-CNR [50].

The O1s spectrum was fitted with three peaks, as shown in Fig. S6a. The deconvoluted peak at 529.6 eV (O1) is attributed to the CeO$_2$ lattice oxygen species (O$_2^-$). Next strong peak (O2) at 531.4 eV is absorbed from the hydroxyl species, defective oxygen, and absorbed surface oxygen. The peak at 532.8 eV (O3) can be attributed to the attached water molecules [51,52]. So, the O1s spectrum implies that the small amount of Co(OH)$_2$ and Ce(OH)$_3$ may exist in the catalyst [40]. However, the CeO$_2$/N–CNR catalyst (Fig. S6b) shows fewer hydroxyl species than Co-CeO$_2$/N-CNR catalysts, which confirms that the hydroxyl species are mostly attached on the surface of Co metal in the carbon nanorods.

3.2.6. Raman analysis

Raman analysis is carried out to understand the nature of carbon, including structural defects for all the catalysts, which is shown in Fig. S7. Raman spectra of all the catalysts are composed of two broad bands at 1330 and 1580 cm^{-1} relate to D and G bands, respectively fitted by Gaussian function [37]. As shown in Fig. S7a, the N-CNR shows the broad D and G band at 1334.7 and 1579.2 cm^{-1} and the intensity ratio of I$_D$/I$_G$ is 1.03. It reveals that the N-CNR has more turbostratic nature and structural defects. However, the Co metal incorporation in the N-CNR (Co/N-CNR) has small positive band shift to 1582.7 cm^{-1}, less band boarding and lower I$_D$/I$_G$ value of 0.86; it explains that the graphitic nature of Co/N-CNR catalyst has increased with decreased structural defects (Fig. S7b). Interestingly, the CeO$_2$ induced N-CNR (Fig. S7c) has similar I$_D$/I$_G$ value (1.03) of N-CNR, as well the negative band shift from Co/N-CNR, it indicates the formation of disordered carbon with more structural defects. In the case of Co-CeO$_2$/N-CNR catalysts (Fig. S7d–f) have more positive peak shift than N-CNR with less band boarding and increased I$_D$/I$_G$ value from 0.86 (Co/N-CNR); it indicates that the carbon in the catalysts consist more structural defects than Co/N-CNR and including the mixed nature of graphitic and amorphous. From these observations, the CeO$_2$ has maintained the amorphous nature of carbon and the structural defects as well, which may be the reason that the Co-CeO$_2$/N-CNR exhibits better catalytic activity than Co/N-CNR.

3.2.7. Elemental analysis (CHNS)

Further, the amount of C and N are quantified by CHNS elemental analysis and tabulated in Table S1. The analysis indicates that the N-CNR and Co/N-CNR catalysts exhibit the same amount of carbon (80 ± 1.55%). But, the CeO$_2$/N-CNR catalyst Exhibits 40.43% of carbon. However, the CeO$_2$ supported Co/N-CNR contains the carbon content of 60 ± 1%. Also, the N-CNR and CeO$_2$/N-CNR has 10.65% and 4.17% of N, which is higher than all other catalysts. However, the Co/N-CNR contains the N content of 2.5%, but, the Co-CeO$_2$/N-CNR catalysts exhibit only ~2%. Thus, the CeO$_2$ incorporation has changed
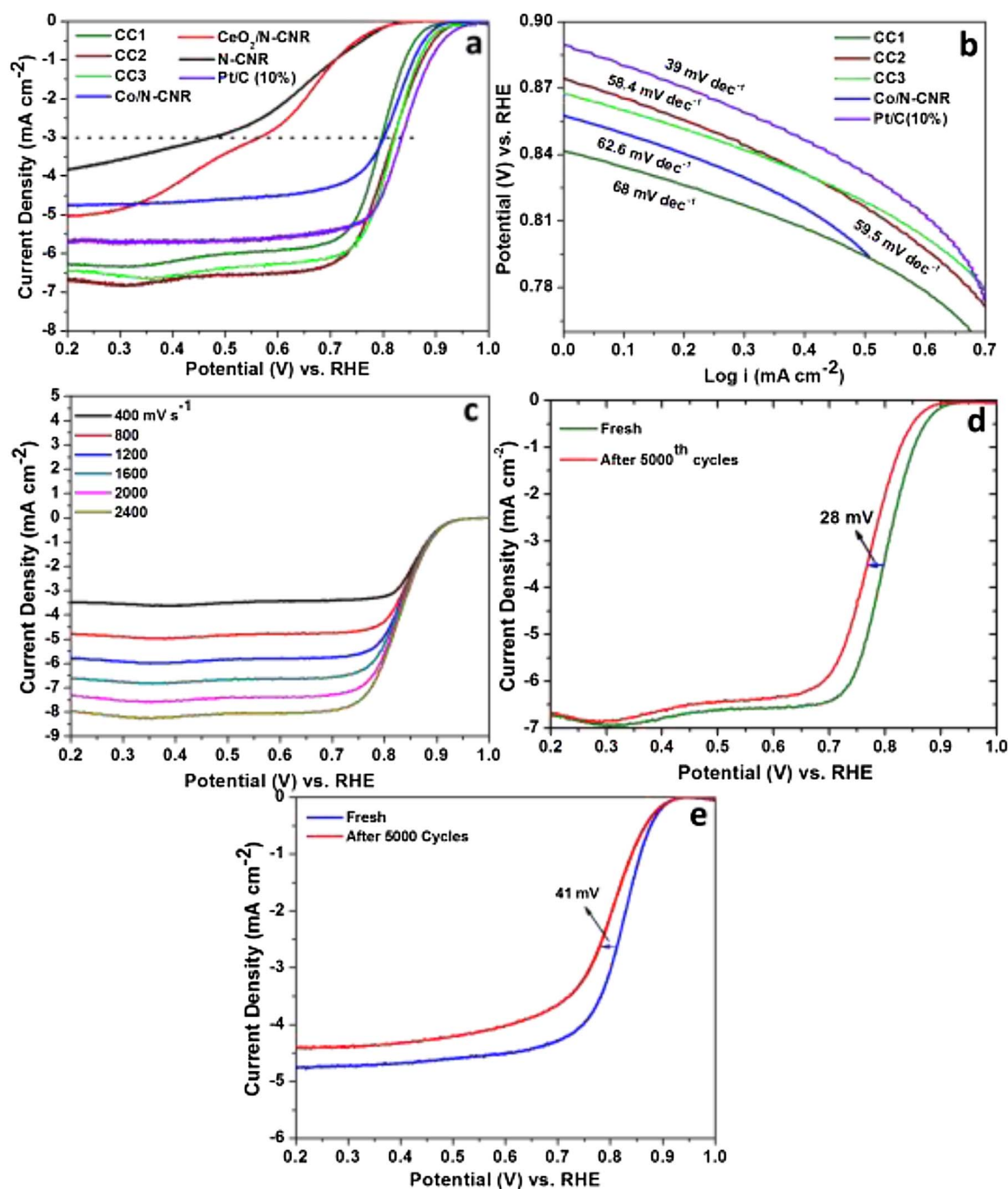
Fig. 7. Oxygen reduction reaction: (a) linear sweep voltammograms, (b) Tafel plots, (c) LSVs at different scan rates from 400 to 2400 mV s^{-1}, and (d, e) cyclic durability test up to 5000 cycles for Co-CeO$_2$/N-CNR, Co/N-CNR catalysts, respectively. All the experiments were carried out at 1600 rpm with 10 mV s^{-1} scan rate in 0.1 M KOH aqueous electrolyte.

the content of both C and N in the Co/N-CNR, which may influence in the catalytic improvement during the electrochemical test.

3.3. Electrochemical performance

3.3.1. Oxygen reduction reaction
3.3.1.1. Linear sweep voltammograms. Based on the above observations, first the CeO$_2$ supported Co/N-CNR is explored as an oxygen reduction reaction catalyst in 0.1 M KOH aqueous electrolyte solution, the obtained results are shown in Figs. 7 and S8 and Table 1. The linear sweep voltammograms (Fig. 7a) display the kinetic and limiting current regions and explains the catalysts behavior during ORR. The N-CNR catalyst shows very low oxygen reduction potential of 0.474 V Vs. RHE

at 3 mA cm^{-2}. But, the CeO$_2$ introduced N-CNR (CeO$_2$/N-CNR) catalyst exhibits the 0.564 V with enriched limiting current density. It indicates that the CeO$_2$ improved the oxygen reduction catalytic activity. Interestingly, the Co/N-CNR catalyst displays the oxygen reduction potential of 0.801 V at 3 mA cm^{-2} current density with the same limiting current density of CeO$_2$/N-CNR. However, once the CeO$_2$ incorporated in Co/N-CNR (Co-CeO$_2$/N-CNR) we can observe the improvement in oxygen reduction potential up to 0.82 V at 3 mA cm^{-2}. The obtained potential from Co-CeO$_2$/N-CNR catalyst is close to the state-of-the-art catalyst of Pt/C(10%), which is 0.834 V. To understand the role of temperature and time we prepared the Co-CeO$_2$/N-CNR catalysts at different conditions, all the catalysts oxygen reduction potential at 3 mA cm^{-2} are listed in Table 1. As shown in

Table 1
Comparison of OER and ORR potentials, Tafel slope values and the oxygen electrode potential for all the catalysts, including reported literature.

Catalysts	OER Potential @ 10 mA cm^{-2} (V)	OER Tafel Slope (mV dec^{-1})	OER Specific Mass Activity (A g^{-1})	ORR Potential @ 3 mA cm^{-2} V)	ORR Tafel Slope (mV dec^{-1})	Oxygen Electrode Potential E_{OER}-E_{ORR} (V)	Ref.
CC1	1.64	90	49.4	0.797	68	0.84	This work
CC2	1.71	102.3	13.9	0.819	58.4	0.89	This work
CC3	1.67	99.5	31.1	0.821	59.5	0.85	This work
Co/N-CNR	1.74	105.8	6.1	0.801	62.6	0.94	This work
CeO$_2$/N-CNR	–	155.7	0.7	0.564	–	–	This work
N-CNR	–	–	0.7	0.474	–	–	This work
Pt/C(10%)	1.87	140.3	5.2	0.834	39	1.036	This work
Co@NPC-900	1.61	–	–	0.76	–	0.85	[57]
Co@Co$_3$O$_4$/C-CM	–	–	–	0.81	–	–	[58]
Co/N-C-800	1.6	61.4	–	0.74	61	0.86	[59]

Fig. 7b, the Tafel plots display the various slope values from their kinetic current and corresponding potential. Among all the catalysts, the Co-CeO$_2$/N-CNR (CC2) catalyst shows the smaller Tafel slope value of 58.4 mV dec^{-1} which is lower than the Co/N-CNR catalyst (62.6 mV dec^{-1}), while the precious catalyst of Pt/C(10%) displays the smaller Tafel slope value of 39 mV dec^{-1} and compared in Table 1.

3.3.1.2. The role of CeO$_2$ in ORR. The CeO$_2$ supported Co/N-CNR catalyst gives the cooperative effect in ORR due to the co-existence of Ce^{4+} and Ce^{3+} ions in CeO$_2$ and their reversible reduction and oxidation states. So, the CeO$_2$ play as an oxygen buffer. According to the report, the oxide species are generated on the Ce^{4+} and lower oxidation state (Ce^{3+}), and which can effectively migrate and reduced on the Co metal surface during ORR process [27,53]. As well, which can absorb more oxygen molecules, and also helps to keep the Co metal with higher valence state, so the maximum number of oxygen molecules are reduced on the Co metal surface through the CeO$_2$ surface [40,49]. Thus, the CeO$_2$ supported catalysts can attain the improvement in both potential and limiting current density.

3.3.1.3. Number electron transfer. Also, the LSVs are performed at different rotation speeds from 400 to 2400 rpm to measure the number of electron transformation during the ORR for both CeO$_2$ supported Co/N-CNR (CC1) and Co/N-CNR catalysts (Figs. 7c and S8a). The current densities are measured at the potentials of 0.65, 0.55, 0.45, 0.35 and 0.25 V and which are plotted versus the rpm ($\omega^{-1/2}$) (Fig. 7c). From the linearly fitted slope value the number electron is calculated with the help of Eq. (1) [54]. The value is found to be ~3.95 for Co-CeO$_2$/N-CNR and ~3.7 for Co/N-CNR, respectively (Fig. S8b and S8c).

3.3.1.4. Cyclic durability tests. Furthermore, to understand the stability of catalyst during ORR, the cyclic durability test (1.1–0.5 V vs. RHE, 50 mV s^{-1} scan rate) is carried out for both Co/N-CNR and CeO$_2$ supported Co/N-CNR catalysts and the LSVs of fresh and after 5000 cycles are displayed in Fig. 6d and e. The CeO$_2$ supported Co/N-CNR (CC1) shows a potential loss of 28 mV at 3 mA cm^{-2} even after 5000 cycles without any limiting current density loss; it implies that 3.5% loss. However after 5000 cycles, the Co/N-CNR electrode Exhibits 41 mV potential loss (more than 5% loss) at 3 mA cm^{-2} (Fig. 7e). So, the interaction between CeO$_2$ and Co in N-CNR may lead the tethering effect; it can efficiently improve the catalyst stability in the electrolyte during the ORR process [16]. The results reveal that the CeO$_2$ is not only enhanced the catalytic performance; it also enhances the stability of the catalyst during the ORR. The cyclic durability test for Pt/C(10%) shows the maximum potential loss of 50 mV (6% loss) after 5000 cycles (Fig. S8d).

3.3.2. Oxygen evolution reaction
3.3.2.1. Linear sweep voltammograms. The oxygen evolution reaction performance is carried out using the same catalysts under the identical conditions to examine the bifunctionality of CeO$_2$ supported Co/N-CNR, and the obtained results are shown in Fig. 8 and compared in Table 1. The OER LSVs from 1.0 to 1.9 V vs. RHE shown in Fig. 8a reveal the importance of CeO$_2$ and its cooperative effect with Co metal in N-CNR towards the enhanced OER activity. The N-CNR and CeO$_2$/N-CNR catalysts show poor OER activity. The Co/N-CNR catalyst exhibits the current density (solar-to-hydrogen) of 10 mA cm^{-2} at the overpotential of 510 mV. However, the Co-CeO$_2$/N-CNR (CC1) affords 10 mA cm^{-2} with an overpotential of 410 mV, which is 100 mV lower than the Co/N-CNR. Furthermore, the state-of-the-art Pt/C(10%) catalyst exhibits overpotential of 640 mV, which is 230 mV higher than the Co-CeO$_2$/N-CNR. Also other controlled catalysts, CC2 and CC3 require 480 and 440 mV overpotential, respectively and both are lower than the Co/N-CNR overpotential at 10 mA cm^{-2} current density.

3.3.2.2. Spillover effect of CeO$_2$ in OER. In general, the oxygen defective
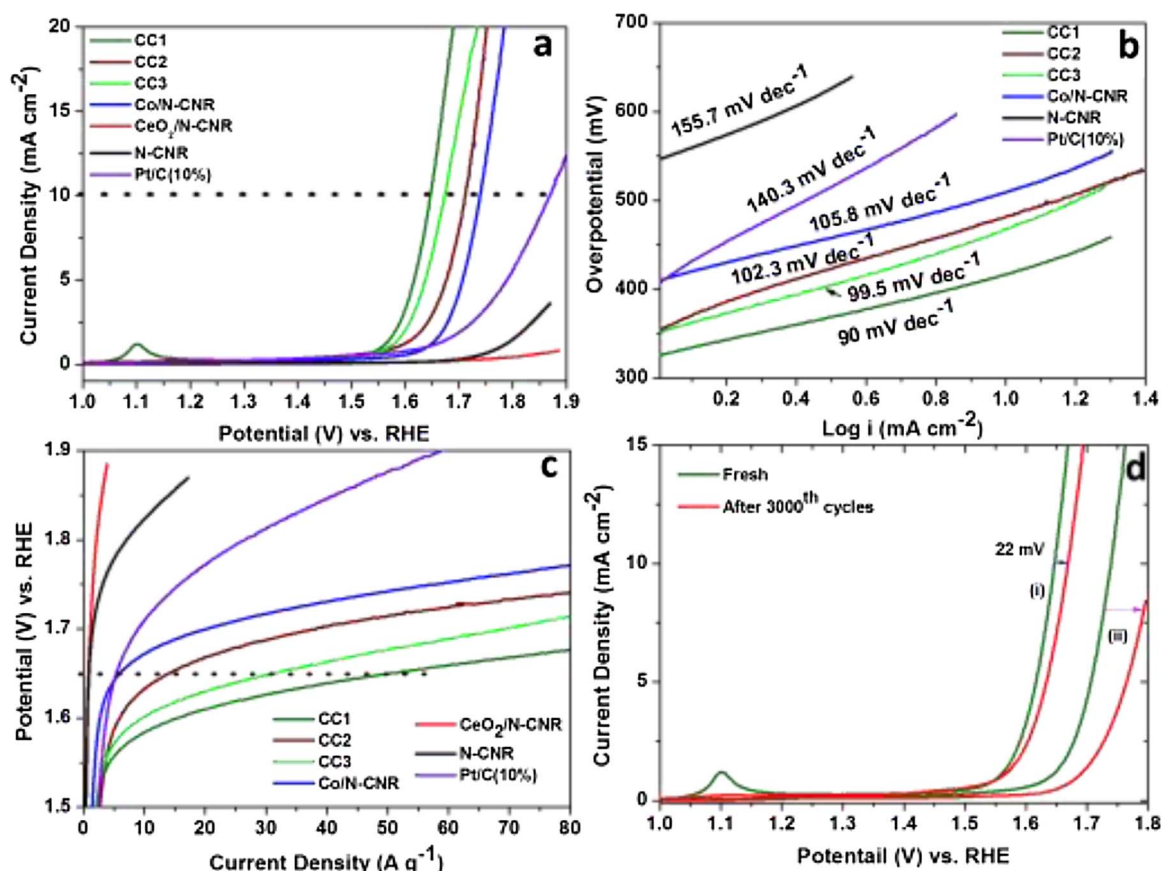
Fig. 8. Oxygen evolution reaction: (a) linear sweep voltammograms, (b) Tafel plots, (c) specific mass activity curves @ 1.65 V vs. RHE and (d) cyclic durability test up to 3000 cycles; (i) Co-CeO$_2$/N-CNR (CC1), and (ii) Co/N-CNR catalysts. All the experiments were carried out at 1600 rpm with 10 mV s^{-1} scan rate in 0.1 M KOH aqueous electrolyte.

ceria can promote the catalytic activity due to the enhanced redox properties of Ce^{4+}/Ce^{3+}, which is confirmed from XPS. So, the highly oxidative species (O$_2^{2-}$/O$^-$) can form on the surface of defective CeO$_2$, mainly because of Ce^{3+} formation and which can easily migrate from CeO$_2$ surface to Co surface by spillover effect [52]. This migrated species can promote the water oxidation [55,29]. As a result, the enhanced OER activity is due to the surface cooperative effect of CeO$_2$ and Co in N-CNR.

3.3.2.3. Tafel slope and specific mass activity. Fig. 7b displays the OER Tafel slope values for various catalysts. The CeO$_2$ supported Co/N-CNR (CC1) catalyst show the less Tafel slope value of 90 mV dec^{-1} than the Tafel slope value of 140.3 mV dec^{-1} for Pt/C(10%) and 105.8 mV dec^{-1} for Co/N-CNR catalysts, which are compared in Table 1. Also, the OER specific mass activities are measured at 1.65 V vs. RHE from Fig. 8c and compared in Table 1. Comparatively, the CeO$_2$ supported Co/N-CNR catalysts exhibit the highest specific mass activities of 49.4 (CC1), 13.9 (CC2) and 31.1 A g^{-1} (CC3) than the 6.1 and 5.2 A g^{-1}) for Co/N-CNR and Pt/C(10%) catalysts, respectively.

3.3.2.4. Cyclic durability tests. To understand the role of CeO$_2$ in the stability of catalyst during OER, the cyclic durability test (1.1–1.7 V vs. RHE, the 100 mV s^{-1} scan rate) is carried out up to 3000 cycles (Fig. 8d). Even after 3000 cycles, the Co-CeO$_2$/N-CNR catalyst ((i) in Fig. 8d) requires additional overpotential of 22 mV to reach the current density of 10 mA cm^{-2}. However, the Co/N-CNR ((ii) in Fig. 8d) catalyst lost the stability more than 70%, even which is not able to reach the current density of 10 mA cm^{-2}. The Co metal is quite unstable in the sluggish OER process. But in the presence of CeO$_2$ the degradation of Co/N-CNR has suppressed and it is possible due to the

maximum adsorption of O$_2^{2-}$/O$^-$ species on the CeO$_2$ surface during the OER process [56].

3.3.2.5. Oxygen electrode potential. The oxygen electrode potentials for various catalysts are calculated [33] from the results of ORR and OER, which is compared in Table 1. In comparison, the Co/N-CNR catalyst shows the higher oxygen-electrode potential of 0.94 V. But, the Co-CeO$_2$/N-CNR catalysts exhibit the lower oxygen electrode potentials of 0.84 V (CC1), 0.89 V (CC2), and 0.85 V (CC3). Furthermore, the commercial catalyst of Pt/C(10%) exhibits 1.036 V oxygen-electrode potential, which is 196 mV higher than the Co-CeO$_2$/N-CNR catalyst. In particular, the CC1 catalyst shows 100 mV lower oxygen electrode potential than Co/N-CNR and the reported values in the literature (Table 1).

3.3.3. Electrochemical active surface area analysis

One of the genuine approaches on electrochemical active sites measurement in the electrolyte is the electrochemical surface area (ECSA) calculation via electrical double layer capacitance (EDLC) using cyclic voltammetry (CV). Accordingly, the ECSA for all the catalysts are measured with various scan rates between 1.24 and 1.34 V vs. RHE [60–62], and results are shown in Figs. 9, S9 and S10 . Fig. 9a displays the CV of Co-CeO$_2$/N-CNR (CC1) catalyst; it reveals that the current has increased by increasing the scan rate. From CV, the anodic and cathodic current is measured at the potential of 1.29 V vs. RHE, and a graph plotted between current versus scan rates (Fig. 9b). The EDLC value has obtained from the slope of the linearly fitted curve, and the calculated EDLC and ECSA values are 0.51 mF and 8.5 cm^2, respectively. In Fig. 9c and d, the Co/N-CNR catalyst exhibits lower EDLC (0.14 mF) and ECSA (2.3 cm^2). Similarly, as shown in Figs. S9 and S10, the ECSA has calculated for all other controlled catalysts and tabulated in Table S2. The
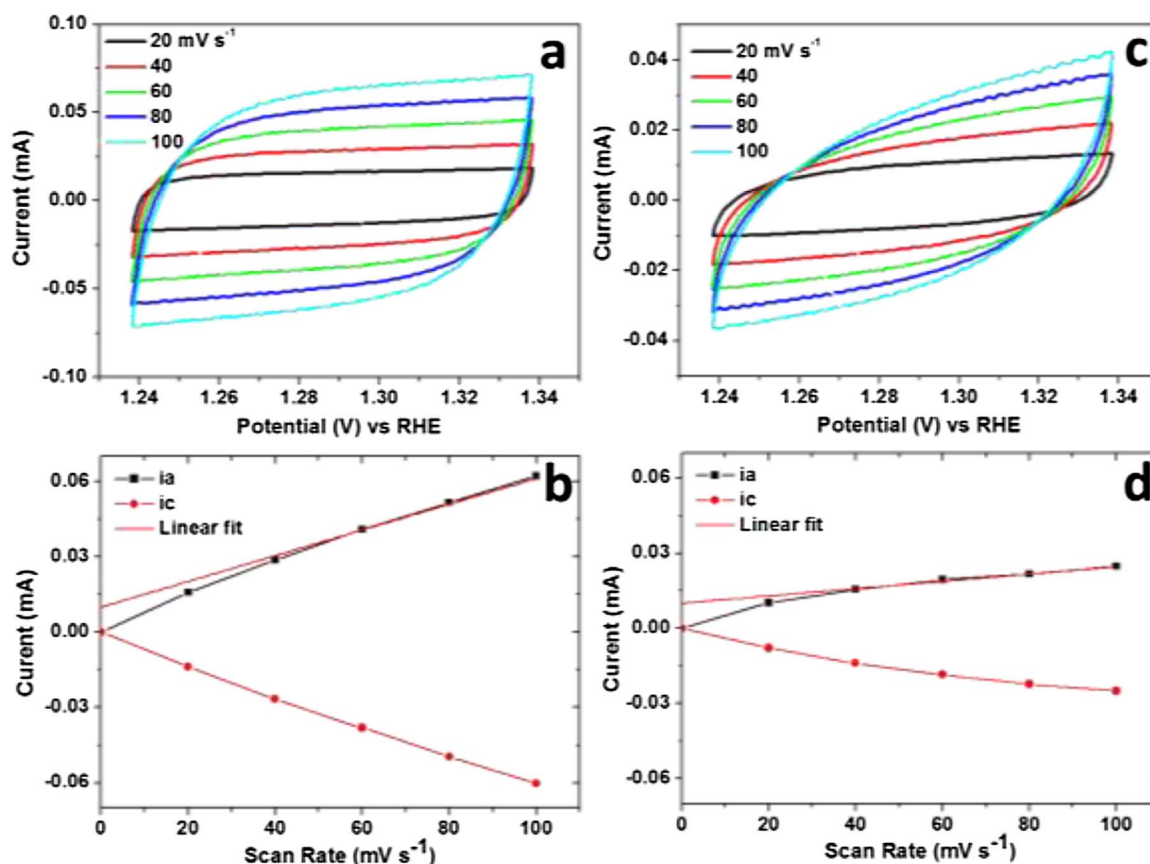
Fig. 9. Electrochemical active surface area measurements: (a) cyclic voltammograms with various scan rates from 20 to 100 mV s^{-1}, (b) scan rates vs. current linear plots (@1.29 vs. RHE) for Co-CeO$_2$/N-CNR (CC1), (c,d) for Co/N-CNR catalysts, in 0.1 M KOH aqueous electrolyte.

Co-CeO$_2$/N-CNR catalyst have the higher ECSA than all other comparison catalysts, including Co/N-CNR catalyst. It indicates that the CeO$_2$ contributes to increase the active sites. These results are in good agreement with BET and FE-SEM analyses results.

3.3.4. Nyquist plots analysis

Nyquist plots of all the catalysts are shown in Fig. 10. The obtained R$_s$ (solution resistance) and R$_{ct}$ (contact resistance) values of each catalyst are compared and tabulated in Table S2. Among all the catalysts, the Co-CeO$_2$/N-CNR catalysts exhibit the lower R$_{ct}$ value (Table

S2), it reveals that the CeO$_2$ in Co/N-CNR has improved the electrical conductivity during the electrochemical reaction. Particularly, Co-CeO$_2$/N-CNR (CC1) catalyst shows very low Rct value of 153 Ω. However, the Co/N-CNR catalyst displays the R$_{ct}$ value of 392 Ω, which is about two times higher than the Co-CeO$_2$/N-CNR (CC1) catalyst. As a result, the electrical conductivity of the catalysts are follow the trend, which is noticed in the electrochemical OER activity. So, it may be one of the reasons that the Co-CeO$_2$/N-CNR catalysts show the better OER activity than all other comparison catalysts, including the Co/N-CNR catalyst.

4. Conclusion

The self-redox Co-CeO$_2$/N-CNR catalyst is fabricated successfully by electro-spun method assisted by annealing. The co-existence of multiple valence states in ceria (Ce^{4+} and Ce^{3+}) are confirmed, and their synergistic effect with cobalt has enhanced the catalytic activity and stability. The Co-CeO$_2$/N-CNR catalyst shows the lower oxygen-electrode potential than the Co/N-CNR, which confirms the bifunctional activity of the Co-CeO$_2$/N-CNR catalyst for enhanced ORR and OER. Also, the stability improvement of Co-CeO$_2$/N-CNR catalyst reveals that the self-redox CeO$_2$ support catalyst can make a dual role in the electrochemical applications. So, this kind of catalysts will make a new direction and impact in the development of new catalysts for energy generation and conversion applications.
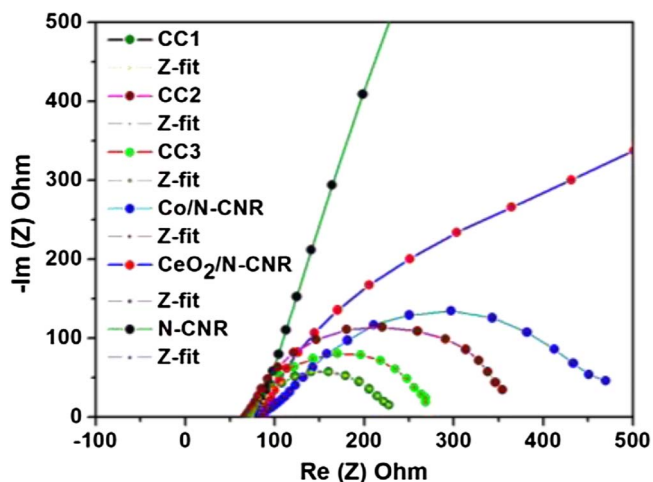

Fig. 10. Electrochemical impedance spectroscopy measurements: Nyquist plots at the applied potential of 1.489 V vs. RHE with the frequency range of 200 kHz–100 mHz for all catalysts in 0.1 M KOH aqueous electrolyte.

for Core Research Facilities (CCRF) in DGIST for the catalyst analyses.

Appendix A. Supplementary data

Supplementary data associated with this article can be found, in the online version, at http://dx.doi.org/10.1016/j.apcatb.2017.08.063.

References

[1] P. Munnik, P.E. de Jongh, K.P. de Jong, Recent developments in the synthesis of supported catalysts, Chem. Rev. 115 (2015) 6687–6718.

[2] D.W. Lee, B.R. Yoo, Advanced metal oxide (supported) catalysts: synthesis and applications, J. Ind. Eng. Chem. 20 (2014) 3947–3959.

[3] T. Sun, L. Xu, S. Li, W. Chai, Y. Huang, Y. Yan, J. Chen, Cobalt-nitrogen-doped ordered macro-/mesoporous carbon for highly efficient oxygen reduction reaction, Appl. Catal. B Environ. 193 (2016) 1–8.

[4] M. Shao, Q. Chang, J.P. Dodelet, R. Chenitz, Recent advances in electrocatalysts for oxygen reduction reaction, Chem. Rev. 116 (2016) 3594–3657.

[5] J. Zhang, Y. Zhao, X. Zhao, Z. Liu, W. Chen, Porous perovskite LaNiO$_3$ nanocubes as cathode catalysts for Li-O$_2$ batteries with low charge potential, Sci. Rep. 4 (2014) 6005.

[6] Y. Cheng, S.P. Jiang, Advances in electrocatalysts for oxygen evolution reaction of water electrolysis-from metal oxides to carbon nanotubes, Prog. Nat. Sci. 25 (2015) 545–553.

[7] J.H. Kim, S. Chang, Y.T. Kim, Compressive strain as the main origin of enhanced oxygen reduction reaction activity for Pt electrocatalysts on chromium-doped titania support, Appl. Catal. B Environ. 158 (2014) 112–118.

[8] J. Masud, S. Umapathi, N. Ashokaan, M. Nath, Iron phosphide nanoparticles as an efficient electrocatalyst for the OER in alkaline solution, J. Mater. Chem. A 4 (2016) 9750–9754.

[9] B.D. Mohapatra, S.P. Mantry, N. Behera, B. Behera, S. Rath, K.S.K. Varadwaj, Stimulation of electrocatalytic oxygen reduction activity on nitrogen doped graphene through noncovalent molecular functionalization, Chem. Commun. 52 (2016) 10385–10388.

[10] A. Pendashteh, J. Palma, M. Anderson, R. Marcilla, NiCoMnO$_4$ nanoparticles on N-doped graphene: highly efficient bifunctional electrocatalyst for oxygen reduction/evolution reactions, Appl. Catal. B Environ. 201 (2017) 241–252.

[11] Z. Ma, S. Dai, Development of novel supported gold catalysts: a materials perspective, Nano Res. 4 (2011) 3–32.

[12] E. Oakton, D. Lebedev, M. Povia, D.F. Abbott, E. Fabbri, A. Fedorov, M. Nachtegaal, C. Coperet, T.J. Schmidt, IrO$_2$-TiO$_2$: a high-surface-area, active, and stable electrocatalyst for the oxygen evolution reaction, ACS Catal. 7 (2017) 2346–2352.

[13] T. Fu, Z. Li, Review of recent development in Co-based catalysts supported on carbon materials for Fischer–Tropsch synthesis, Chem. Eng.Sci. 135 (2015) 3–20.

[14] J.Q. Bond, D.M. Alonso, D. Wang, R.M. West, J.A. Dumesic, Integrated catalytic conversion of γ-valerolactone to liquid alkenes for transportation fuels, Science 327 (2010) 1110–1114.

[15] B. Peng, X. Yuan, C. Zhao, J.A. Lercher, Stabilizing catalytic pathways via redundancy: selective reduction of microalgae oil to alkanes, J. Am. Chem. Soc. 134 (2012) 9400–9405.

[16] D. Higgins, P. Zamani, A. Yu, Z. Chen, The application of graphene and its composites in oxygen reduction electrocatalysis: a perspective and review of recent progress, Energy Environ. Sci. 9 (2016) 357–390.

[17] D. Higgins, M.A. Hoque, M.H. Seo, R. Wang, F. Hassan, J.Y. Choi, M. Pritzker, A. Yu, J. Zhang, Z. Chen, Development and simulation of sulfur-doped graphene supported Platinum with exemplary stability and activity towards oxygen reduction, Adv. Funct. Mater. 24 (2014) 4325–4336.

[18] C. Sun, H. Li, L. Chen, Nanostructured ceria-based materials: synthesis, properties, and applications, Energy Environ. Sci. 5 (2012) 8475–8505.

[19] N. Laosiripojana, S. Assabumrungrat, Catalytic steam reforming of ethanol over high surface area CeO$_2$: the role of CeO$_2$ as an internal pre-reforming catalyst, Appl. Catal. B Environ. 66 (2006) 29–39.

[20] J. Qi, K. Zhao, G. Li, Y. Gao, H. Zhao, R. Yu, Z. Tang, Multi-shelled CeO$_2$ hollow microspheres as superior photocatalysts for water oxidation, Nanoscale 6 (2014) 4072–4077.

[21] K. Zhao, J. Qi, H. Yin, Z. Wang, S. Zhao, X. Ma, J. Wan, L. Chang, Y. Gao, R. Yu, Z. Tang, Efficient water oxidation under visible light by tuning surface defects on ceria nanorods, J. Mater. Chem. A 3 (2015) 20465–20470.

[22] S. Sanna, V. Esposito, J.W. Andreasen, J. Hjelm, W. Zhang, T. Kasama, S.B. Simonsen, M. Christensen, S. Linderoth, N. Pryds, Enhancement of the chemical stability in confined δ-Bi$_2$O$_3$, Nat. Mater. 14 (2015) 500–504.

[23] J.A. Rodriguez, S Ma, P. Liu, J. Hrbek, J. Evans, M. Perez, Activity of CeO$_x$ and TiO$_x$ nanoparticles grown on Au(111) in the water-gas shift reaction, Science 318 (2007) 1757–1760.

[24] X.H. Guo, C.C. Mao, J. Zhang, J. Huang, W.N. Wang, Y.H. Deng, Y.Y. Wang, Y. Cao, W.X. Huang, S.H. Yu, Cobalt-doping-induced synthesis of ceria nanodisks and their significantly enhanced catalytic activity, Small 8 (2012) 1515–1520.

[25] X. Liu, K. Zhou, L. Wang, B. Wang, Y. Li, Oxygen vacancy clusters promoting reducibility and activity of ceria nanorods, J. Am. Chem. Soc. 131 (2009) 3140–3141.

[26] J.J. Yang, F. Miao, M.D. Pickett, D.A.A. Ohlberg, D.R. Stewart, C.N. Lau, R.S. Williams, The mechanism of electroforming of metal oxide memristive switches, Nanotechnology 20 (2009) 215201–215209.

[27] X. Lin, L. Zhou, T. Huang, A. Yu, Cerium oxides as oxygen reduction catalysts for

[28] Lithium-Air batteries, Int. J. Electrochem. Sci. 7 (2012) 9550–9559.

[28] J. Kim, Z.K. Ghouri, R.Z. Khan, T. An, M. Park, H.Y. Kim, Experimental study on synthesis of Co/CeO$_2$-doped carbon nanofibers and its performance in supercapacitors, Carbon Lett. 16 (2015) 270–274.

[29] F. Liang, Y. Yu, W. Zhou, X. Xu, Z. Zhu, Highly defective CeO$_2$ as a promoter for efficient and stable water oxidation, J. Mater. Chem. A 3 (2015) 634–640.

[30] H. Mistry, A.S. Varela, C.S. Bonifacio, I. Zegkinoglou, I. Sinev, Y.W. Choi, K. Kisslinger, E.A. Stach, J.C. Yang, P. Strasser, B.R. Cuenya, Highly selective plasma-activated copper catalysts for carbon dioxide reduction to ethylene, Nat. Commun. 7 (2016) 12123.

[31] Z. Li, F. Han, C. Li, X. Jiao, D. Chen, Hollow CeO$_2$ dodecahedrons: one-step template synthesis and enhanced catalytic performance, RSC Adv. 6 (2016) 60975–60982.

[32] P. Ramakrishnan, S. Shanmugam, Cobalt nanoparticles embedded nitrogen doped carbon nanorods as a high performance electrode material for supercapacitor applications, Electrochim. Acta 125 (2014) 232–240.

[33] P. Ganesan, M. Prabu, J. Sanetuntikul, S. Shanmugam, Cobalt sulfide nanoparticles grown on nitrogen and sulfur codoped graphene oxide: an efficient electrocatalyst for oxygen reduction and evolution reactions, ACS Catal. 5 (2015) 3625–3637.

[34] G. Wu, N.H. Mack, W. Gao, S. Ma, R. Zhong, J. Han, J.K. Baldwin, P. Zelenay, Nitrogen-doped graphene-rich catalysts derived from heteroatom polymers for oxygen reduction in nonaqueous Lithium-O$_2$ battery cathodes, ACS Nano 11 (2012) 9764–9776.

[35] W. Yihong, S. Zexiang, Y. Ting, Two-Dimensional Carbon: Fundamentals Properties, Synthesis, Characterization, and Applications, Taylor & Francis Group, USA, 2014, pp. 1–346.

[36] G. Lota, K. Fic, E. Frackowiak, Carbon nanotubes and their composites in electrochemical applications, Energy Environ. Sci. 4 (2011) 1592–1605.

[37] E. Tatarova, A. Dias, J. Henriques, A.M.B.D. Rego, A.M. Ferraria, M.V. Abrashev, C.C. Luhrs, J. Phillips, F.M. Dias, C.M. Ferreira, Microwave plasmas applied for the synthesis of free standing graphene sheets, J. Phys. D: Appl. Phys. 47 (2014) 385501.

[38] A.P. Dementjev, K.I. Maslakov, Possibilities of C 1s XPS and N(E) C KVV Auger spectroscopy for identification of inherent peculiarities of diamond growth, Appl. Surf. Sci. 253 (2006) 1095–1100.

[39] B. Kumar, M. Asadi, D. Pisasale, S.S. Ray, B.A. Rosen, R. Haasch, J. Abiade, A.L. Yarin, A.S. Khojin, Renewable and metal-free carbon nanofiber catalysts for carbon dioxide reduction, Nat. Commun. 4 (2013) 2819.

[40] H. Dong, C. Liu, H. Ye, L. Hu, B. Fugetsu, W. Dai, Y. Cao, X. Qi, H. Lu, X. Zhang, Three-dimensional nitrogen-doped graphene supported molybdenum disulfide nanoparticles as an advanced catalyst for hydrogen evolution reaction, Sci. Rep. 5 (2015) 17542.

[41] J. Sanetuntikul, C. Chuaicham, J.W. Choi, S. Shanmugam, Investigation of hollow nitrogen-doped carbon spheres as non-precious Fe-N$_4$ based oxygen reduction catalyst, J. Mater. Chem. A 3 (2015) 15473–15481.

[42] N.P. Wickramaratne, J. Xu, M. Wang, L. Zhu, L. Dai, M. Jaroniec, Nitrogen enriched porous carbon spheres: attractive materials for supercapacitor electrodes and CO$_2$ adsorption, Chem. Mater. 26 (2014) 2820–2828.

[43] H. Schmiers, J. Friebel, P. Streubel, R. Hesse, R. Kopsel, Change of chemical bonding of nitrogen of polymeric N-heterocyclic compounds during pyrolysis, Carbon 37 (1999) 1965–1978.

[44] S. Zhao, B. Rasimick, W. Mustain, H. Xu, Highly durable and active Co$_3$O$_4$ nanocrystals supported on carbon nanotubes as bifunctional electrocatalysts in alkaline media, Appl. Catal. B Environ. 203 (2017) 138–145.

[45] M.C. Biesinger, B.P. Payne, L.W.M. Lau, A. Gerson, R.S.C. Smart, X-ray photoelectron spectroscopic chemical state quantification of mixed nickel metal, oxide and hydroxide systems, Surf. Interface Anal. 41 (2009) 324–332.

[46] A. Sivanantham, P. Ganesan, S. Shanmugam, Hierarchical NiCo$_2$S$_4$ nanowire arrays supported on Ni Foam: an efficient and durable bifunctional electrocatalyst for oxygen and hydrogen evolution reactions, Adv. Funct. Mater. 26 (2016) 4661–4672.

[47] J. Cui, X. Zhang, L. Tong, J. Luo, Y. Wang, Y. Zhang, K. Xie, Y. Wu, A facile synthesis of mesoporous Co$_3$O$_4$/CeO$_2$ hybrid nanowire arrays for high performance supercapacitors, J. Mater. Chem. A 3 (2015) 10425–10431.

[48] A. Younis, D. Chu, S. Li, Oxygen level: the dominant of resistive switching characteristics in cerium oxide thin films, J. Phys. D: Appl. Phys. 45 (2012) 355101–355106.

[49] Y. Chen, S. Zhao, Z. Liu, Influence of the synergistic effect between Co–N–C and ceria on the catalytic performance for selective oxidation of ethylbenzene, Phys. Chem. Chem. Phys. 17 (2015) 14012–14020.

[50] L.F. Liotta, G.D. Carlo, G. Pantaleo, A.M. Venezia, G. Deganello, Co$_3$O$_4$/CeO$_2$ composite oxides for methane emissions abatement: relationship between Co$_3$O$_4$–CeO$_2$ interaction and catalytic activity, Appl. Catal. B Environ. 66 (2006) 217–227.

[51] X. Liu, H. Yang, L. Han, W. Liu, C. Zhang, X. Zhang, S. Wang, Y. Yang, Mesoporous-shelled CeO$_2$ hollow nanospheres synthesized by a one-pot hydrothermal route and their catalytic performance, CrystEngComm 15 (2013) 7769–7775.

[52] L. Xue, C. Zhang, H. He, Y. Teraoka, Catalytic decomposition of N$_2$O over CeO$_2$ promoted Co$_3$O$_4$ spinel catalyst, Appl. Catal. B Environ. 75 (2007) 167–174.

[53] S.A. Freunberger, Y. Chen, Z. Peng, J.M. Griffin, L.J. Hardwick, F. Barde, P. Novak, P.G. Bruce, Reactions in the rechargeable Lithium-O$_2$ battery with alkyl carbonate electrolytes, J. Am. Chem. Soc. 133 (2011) 8040–8047.

[54] J. Sanetuntikul, S. Shanmugam, High pressure pyrolyzed non-precious metal oxygen reduction catalysts for alkaline polymer electrolyte membrane fuel cells, Nanoscale 7 (2015) 7644–7650.

[55] S. Wodiunig, F. Bokeloh, J. Nicole, C. Comninellis, Electrochemical promotion of RuO$_2$ catalyst dispersed on an Yttria-Stabilized Zirconia monolith, Electrochem.

Solid State Lett. 2 (1999) 281–283.

[56] V.I. Markoulaki, I.T. Papadas, I. Kornarakis, G.S. Armatas, Synthesis of ordered mesoporous CuO/CeO₂ composite frameworks as anode catalysts for water oxidation, Nanomaterials 5 (2015) 1971–1984.

[57] H.S. Lu, H. Zhang, R. Liu, X. Zhang, H. Zhao, G. Wang, Macroscale cobalt-MOFs derived metallic Co nanoparticles embedded in N-doped porous carbon layers as efficient oxygen electrocatalysts, Appl. Surf. Sci. 392 (2017) 402–409.

[58] W. Xia, R. Zou, L. An, D. Xia, S. Guo, A metal–organic framework route to in situ encapsulation of Co@Co₃O₄@C core@bishell nanoparticles into a highly ordered porous carbon matrix for oxygen reduction, Energy Environ. Sci. 8 (2015) 568–576.

[59] Y. Su, Y. Zhu, H. Jiang, J. Shen, X. Yang, W. Zou, J. Chen, C. Li, Cobalt nanoparticles

embedded in N-doped carbon as an efficient bifunctional electrocatalyst for oxygen reduction and evolution reactions, Nanoscale 6 (2014) 15080–15089.

[60] A. Sivanantham, S. Shanmugam, Nickel selenide supported on nickel foam as an efficient and durable non-precious electrocatalyst for the alkaline water electrolysis, Appl. Catal. B Environ. 203 (2017) 485–493.

[61] J. Sanetuntikul, K. Ketpang, S. Shanmugam, Hierarchical nanostructured Pt₈Ti-TiO₂/C as an efficient and durable anode catalyst for direct methanol fuel cells, ACS Catal. 5 (2015) 7321–7327.

[62] X. Peng, S. Zhao, T.J. Omasta, J.M. Roller, W.E. Mustain, Activity and durability of Pt-Ni nanocage electocatalysts in proton exchange membrane fuel cells, Appl. Catal. B Environ. 203 (2017) 927–935.